RSC Advances

PAPER

View Article Online
View Journal | View Issue



Cite this: *RSC Adv.*, 2017, **7**, 36101

# Construction of $SnO_2$/graphene-like g-$C_3N_4$ with enhanced visible light photocatalytic activity†

Haiyan Ji,[a] Yamin Fan,[a] Jia Yan,[b] Yuanguo Xu,[b] Xiaojie She,[a] Jiemin Gu,[a] Ting Fei,[a] Hui Xu*[a] and Huaming Li*[a]

Received 24th May 2017
Accepted 13th July 2017

DOI: 10.1039/c7ra05830f

rsc.li/rsc-advances

In this work, $SnO_2$/graphene-like g-$C_3N_4$ ($SnO_2$/GL-$C_3N_4$) composite photocatalysts with large surface areas and abundant coupling heterointerfaces were synthesized using a hydrothermal method. The as-prepared photocatalysts exhibited distinctly manifested efficient visible light activities toward organic pollutant degradation, demonstrating remarkable synergistic effects between $SnO_2$ and graphene-like g-$C_3N_4$ (GL-$C_3N_4$). The 25 wt% $SnO_2$/GL-$C_3N_4$ composite showed optimal photocatalytic activity under visible light irradiation, which was almost 9 and 2.5 times as high as that of $SnO_2$ and GL-$C_3N_4$, respectively. In addition, the possible photocatalytic mechanism of rhodamine B (RhB) degradation by $SnO_2$/GL-$C_3N_4$ under visible light was also discussed in detail. Moreover, this work would provide a facile way for the fabrication of novel two dimension/two dimension (2D/2D) GL-$C_3N_4$-based photocatalysts with high and stable performance for pollutant degradation.



## 1. Introduction

Currently, with the rapid development of global industrialization, industrial wastewater treatment has become a big problem. Many measures have been used to alleviate the environmental issues. Photocatalysis with clean and economical energy has revealed wide prospects in application for the treatment of organic wastewater. Therefore, using semiconductor-based photocatalysts for the degradation of organic pollutants is considered as a sustainable and prospective solution for wastewater purification.[1]

Graphitic carbon nitride (g-$C_3N_4$) is a promising heterogeneous metal-free, non-toxic semiconductor with narrow band gap, good thermal stability, high chemical stability and interesting electronic properties,[2,3] has been widely researched for catalysis-driven application,[4,5] electrochemical application,[6] bio-chemical application,[7] biosensor application[8] and so on. And yet, it is found that the layered stacking structure and small specific surface area of g-$C_3N_4$ hinder the effective separation of photoinduced electron–hole pairs, thus made g-$C_3N_4$ suffering from rapid recombination of photogenerated electron–hole pairs. Therefore, researchers have made great efforts to solve these problems. It is well known that two dimension (2D) materials have advantages: (1) atomic thickness which could shorten the routine that photogenerated electrons and holes had to pass in order to participate in the photocatalytic reaction quickly, (2) large surface areas that could expose more active sites.[9–12] Indeed, it has been reported that g-$C_3N_4$ could be easily exfoliated into 2D graphene-like g-$C_3N_4$ nanosheets (GL-$C_3N_4$)[13] with larger surface area and high photocatalytic activity.[14,15] The obtained GL-$C_3N_4$ had a typical 2D structure with thickness of 2–3 nm and band gap of 2.85 eV, exhibited excellent performance in catalysis.[10] However, the visible light photocatalytic activity of GL-$C_3N_4$ doesn't meet expectations,[16] therefore, continue to decrease the high recombination rate of photogenerated electrons and holes of GL-$C_3N_4$ is necessary. Lately, 2D/2D materials have attracted extensive attention due to (1) enlarged contact area in interface region that could accelerate the charge carrier separation and inhibit its recombination,[17,18] (2) forming a low Schottky barrier height junction which could reduce contact resistance and facilitate carrier transport.[19] It is obvious that combining GL-$C_3N_4$ with other 2D materials forming 2D/2D structures so as to obtain more surface area and high coupling heterointerfaces extent, that could effectively facilitate separation/transfer of photoinduced electron–hole pairs, and thus improve the catalytic performance of GL-$C_3N_4$.[18] Several studies have proven that combining g-$C_3N_4$ nanosheet with other 2D materials to form 2D/2D structures can indeed efficiently suppressed the recombination of photoinduced electron–hole pairs, endues the composites with enhanced properties as a result of the synergistic effects see in carbonized poly(furfural alcohol)/g-$C_3N_4$,[17] rGO/g-$C_3N_4$,[20] $SnNb_2O_6$/g-$C_3N_4$.[18]

$SnO_2$, a n-type semiconductor, has become one of the hot spots in the field of photocatalysis research attributed to its high photosensitivity, good transparency, environmental

[a]School of Materials Science and Engineering, Institute for Energy Research, Jiangsu University, Zhenjiang 212013, China. E-mail: xh@ujs.edu.cn

[b]School of Chemistry and Chemical Engineering, Jiangsu University, Zhenjiang 212013, China

† Electronic supplementary information (ESI) available. See DOI: 10.1039/c7ra05830f

friendliness and low cost.[21] $SnO_2$ based semiconductors such as $Fe_2O_3/SnO_2$,[22] $CuO–SnO_2$,[23] $SnO_2/TiO_2$,[24] $SnO/SnO_2$,[25] $SnO_2/Fe_2O_3$,[26] $SnO_2/ZnS$[21] showed stable and outstanding performances in photocatalysis. Especially, 2D $SnO_2$ nanosheets can provide many promising properties for improving photocatalytic performance, which to a large extent benefit from their confined thickness and large specific surface. The existing literature proved that compounding $SnO_2$ nanosheets with other suitable materials forming composites with intimate connection and continuity in lattice, like $SnO_2$ nanosheets–CdSe nanocrystallites,[27] porous $ZnO–SnO_2$ nanosheets,[28] could help for facilitating the separations of photoinduced electron–hole pairs more effectively. However, there are few reports coupling GL-$C_3N_4$ with $SnO_2$ nanosheet together as to construct 2D/2D $SnO_2$ nanosheets/graphene-like g-$C_3N_4$ ($SnO_2$/GL-$C_3N_4$) in order to enhance photocatalytic performance for both GL-$C_3N_4$ and $SnO_2$ in the visible light region.

In this work, we report novel hybrid architecture of $SnO_2$/GL-$C_3N_4$ for photocatalytic environmental application. The $SnO_2$/GL-$C_3N_4$ photocatalysts were synthesized by an environmentally friendly hydrothermal method *via* the *in situ* growth of GL-$C_3N_4$ in the presence of $SnO_2$ nanosheets. The visible-light-driven photocatalytic activities of $SnO_2$/GL-$C_3N_4$ composites were evaluated by the degradation of RhB. It has been found that the optimal photocatalytic activity over 25 wt% $SnO_2$/GL-$C_3N_4$ was almost 9 times as high as that of $SnO_2$ precursor, and 2.5 times higher than that of GL-$C_3N_4$ precursor, respectively. The crystal structure, chemical state of elements, chemical composition, structural information, microstructure and grain morphology of the synthesized photocatalysts were analyzed by X-ray diffraction (XRD), X-ray photoelectron spectra (XPS), Fourier transform infrared spectra (FT-IR), scanning electron microscopy (SEM) and transmission electron microscopy (TEM), respectively. In addition, photoluminescence (PL) spectra, transient photocurrent response and electrochemical impedance spectroscopy (EIS) analysis also demonstrated that the introduction of $SnO_2$ could decrease the high recombination rate of photogenerated electron–hole pairs, which would consequently improve the visible-light photo-catalytic activity of GL-$C_3N_4$.

## 2. Experimental section

### 2.1. Materials

Stannous chloride ($SnCl_2 \cdot 2H_2O$, A.R. grade), ammonia solution ($NH_3 \cdot H_2O$, A.R. grade), dicyandiamide ($C_2H_4N_4$, C.P. grade), ethanol ($C_2H_5OH$, A.R. grade), ammonium chloride ($NH_4Cl$, A.R. grade), all the starting materials were used directly without purification.

### 2.2. Material synthesis

$SnO_2$ nanosheets,[29] g-$C_3N_4$ and GL-$C_3N_4$ (ref. 13) were synthesized according to the reported procedure. The $SnO_2$/GL-$C_3N_4$ photocatalysts were synthesized by hydrothermal method. In this process, 0.015 g $SnO_2$, 0.1 g g-$C_3N_4$ and 0.5 g $NH_4Cl$ were added into 40 mL solvent composed of 10 mL alcohol and 30 mL deionized water under vigorous stirring and ultrasonication for 1 h. Afterwards, the mixture was transferred into 50 mL Teflon-lined autoclave, and putted into a 180 °C drying oven for 12 h. At last, the photocatalyst was collected by centrifugation, washing with ethanol and distilled water repeatedly, and frozen drying for 12 h. The obtained product was 15 wt% $SnO_2$/GL-$C_3N_4$. Different weight percent (15 wt%, 25 wt%, 35 wt%) of $SnO_2$/GL-$C_3N_4$ photocatalysts were synthesized with the similar procedure.

### 2.3. Characterization

The compositions and crystal structure of the as-prepared samples were analyzed by XRD obtained on a Bruker D8 diffractometer using Cu K$\alpha$ radiation ($\lambda = 1.5418$ Å) in $2\theta$ range of 10–80° with the scanning rate of 7° $min^{-1}$. The nitrogen adsorption–desorption isotherms were recorded on a TriStar II 3020 surface area and porosity analyzer. XPS was used to further determine the composition and electronic state of the $SnO_2$ nanosheets, GL-$C_3N_4$ and $SnO_2$/GL-$C_3N_4$ using an ESCA Lab MKII X-ray photo-electron spectrometer using Mg K$\alpha$ radiation. FT-IR was performed on a FT-IR Nexus 470 spectrometer, taking with KBr as standard material at room temperature to reveal the structural information of obtained samples. The compositions and morphologies of the samples were observed by SEM, TEM, high resolution transmission electron microscope (HRTEM), elemental mapping and energy-dispersive X-ray spectroscopy (EDS). And SEM, elemental mapping, EDS were taken with a JEOL-JSM-7001F while TEM, HRTEM were operated at 200 kV on a JEOL-JEM-2010 made in Japan. Ultraviolet-visible (UV-vis) diffuse reflection spectra (DRS) of the samples were recorded on an UV-2425 UV-vis spectrophotometer made in Shimadzu, Japan from the range of 200 nm to 800 nm, and $BaSO_4$ was employed as a reflectance standard. Photocurrents and EIS were performed at a CHI 660B electro-chemical workstation made in Chenhua Instrument Company (Shanghai, China). PL experiments were obtained on QuantaMaster & TimeMaster Spectrofluorometer using excitation wavelength at 387 nm and 275 nm, respectively. X-band equivalent series resistance (ESR) spectra were measured by a JES FA200 spectrometer at ambient temperature, operating at 9.5 GHz.

### 2.4. Photocatalytic experiments

Photocatalytic activities of the as-synthesized catalysts were assessed by photocatalytical degradation of RhB irradiated under the visible light in a custom-made photochemical reactor with air bubbling. 50 mg of the photocatalyst powder was directly dispersed in 50 mL of RhB aqueous solution (10 mg $L^{-1}$) with continuous stirring at 30 °C. At first, all the suspensions were continuously stirred for half an hour in dark condition, in order to establish an adsorption/desorption balance. Then open the spherical Xe lamp (300 W) with a cut-off light filter ($\lambda > 420$ nm) which was used as visible light source. At every 30 min, about 4.0 mL solution suspension would be taken out and detected by a UV-vis spectrophotometer (Cary, 8584; NYSE:A) at 553 nm which is the characteristic maximum absorption

 

wavelength of RhB. The following formula (eqn (1)) was used to obtain the photocatalytic degradation efficiency ($E$) of RhB:

$$E = \left(1 - \frac{C}{C_0}\right) \times 100\% = \left(1 - \frac{A}{A_0}\right) \times 100\% \quad (1)$$

where $C_0$, $A_0$ is the concentration of solution supernatant with an adsorption/desorption equilibrium at the initial reaction time, and the corresponding values of absorbance, respectively; $C$, $A$ is the concentration of solution supernatant, and the corresponding values of absorbance at time $t$, respectively. In this work, we use the values of absorbance between 400–600 nm to obtain the photocatalytic degradation efficiency of RhB.

### 2.5. Photoelectrochemical measurements

Photocurrents were measured in a standard three-electrode experimental system, employing a Pt wire as the counter electrode and the sample modified indium-tin oxide glass (ITO) as the working electrode while a saturated Ag/AgCl electrode as the reference electrode. Phosphate buffered saline (PBS, pH = 7.0) was used as the supporting electrolyte solution of photocurrent measurements and the light source was a 500 W Xe arc lamp. GL-$C_3N_4$, $SnO_2$ and $SnO_2$/GL-$C_3N_4$ electrodes were prepared with the procedure: At first, dispersing 5.0 mg sample powder in 1.0 mL ethylene glycol by ultrasound. Afterward, 20 μL as-prepared dispersion (5 mg $mL^{-1}$) was one-off drop-cast onto a piece of ITO (0.5 × 1 $cm^2$) with the infrared lamp irradiation, as to form the sample modified ITO electrode. EIS of different electrodes were measured in 0.1 M KCl solution containing 5 mM $K_4[Fe(CN)_6]/K_3[Fe(CN)_6]$ under sunless conditions. And every Nyquist plot was recorded in frequency range of 100 MHz to 100 kHz.

## 3. Results and discussion

### 3.1. XRD, FT-IR analyses

The XRD patterns of the GL-$C_3N_4$, $SnO_2$ and $SnO_2$/GL-$C_3N_4$ samples with different weight percent of $SnO_2$ were shown in Fig. 1(a). It could be seen that the peaks of $SnO_2$/GL-$C_3N_4$ were distinctly similar to that of $SnO_2$, indicating that $SnO_2$ has no obvious change during the material preparation. In addition, the $SnO_2$/GL-$C_3N_4$ composites showed the sole $SnO_2$ peaks without the GL-$C_3N_4$ peak owing to the reason that, the peak of (002) crystal plane of GL-$C_3N_4$ maybe overlapped with the peak of (110) crystal plane of $SnO_2$ since the two were very close. The pure $SnO_2$ exhibited several peaks at $2\theta$ = 26.7°, 33.7°, 38.1°, 51.8°, 54.9°, 61.7°, 65.4°, 71.1° and 78.4° corresponding to (110), (101), (200), (211), (220), (310), (301), (202) and (321) plane of a tetragonal rutile-like $SnO_2$.[29,30] The strong and sharp peak at $2\theta$ = 27.8° could be corresponded to the (002) diffraction plane of GL-$C_3N_4$, this is consistent with the reported literature.[1] No impurity peaks in GL-$C_3N_4$, $SnO_2$ and $SnO_2$/GL-$C_3N_4$, indicating that those photocatalysts were successfully prepared in this work.

The FT-IR spectrum enables us to distinguish the molecular structure of $SnO_2$, GL-$C_3N_4$ and $SnO_2$/GL-$C_3N_4$ composites (Fig. 1(b)). With regard to the $SnO_2$/GL-$C_3N_4$ composites, both GL-$C_3N_4$ and $SnO_2$ could be detected confirming the $SnO_2$/GL-$C_3N_4$ composites were successful synthesized. The peaks at 807, 1100–1650, 2400 $cm^{-1}$ in the GL-$C_3N_4$ spectrum corresponded to the unique breathing mode of triazine units,[31–33] characteristic stretching modes of the C=N and C–N heterocycles,[31] adsorption of $CO_2$ in the environment, respectively. And the broad band at 3000–3600 $cm^{-1}$ was attributed to the residual N–H group.[34] $SnO_2$ showed only a broad strong peak at 400–700 $cm^{-1}$, which could be ascribed to the anti-symmetric stretching vibration of Sn–O–Sn.[25,35,36] Compared with pure $SnO_2$, the band at 597 $cm^{-1}$ was red-shifted in $SnO_2$/GL-$C_3N_4$ composites, suggesting that there were interactions between $SnO_2$ and GL-$C_3N_4$.

### 3.2. XPS analysis

XPS analyses were conducted to determine the composition and surface electronic state of $SnO_2$, GL-$C_3N_4$ and 25 wt% $SnO_2$/GL-$C_3N_4$ composite. As shown in Fig. 2(a), $SnO_2$ was composed of Sn, O elements and for the pure GL-$C_3N_4$, only C and N elements were detected, while the 25 wt% $SnO_2$/GL-$C_3N_4$ was composed of C, N, Sn and O elements. High-resolution of C 1s, N 1s, Sn 3d and O 1s spectra of the material were plotted in Fig. 2(b)–(e) in details. It could be observed in Fig. 2(b) that C 1s for GL-$C_3N_4$ had two peaks at 288.2 and 284.7 eV. The peak at 284.7 eV due to carbon contamination which could be observed on the XPS characterization for all samples in Fig. 2(b), while the C 1s at 288.2 eV was associated with $sp^2$-bonded carbon (N–C=N) which had been shift to 288.4 eV in 25 wt% $SnO_2$/GL-$C_3N_4$.[31,37,38] The shift of C 1s at 288.4 eV in 25 wt% $SnO_2$/GL-$C_3N_4$ could be

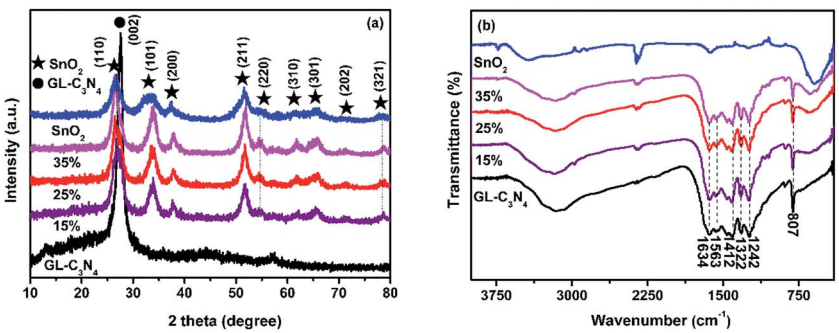


Fig. 1 (a) XRD patterns, (b) FT-IR spectra of $SnO_2$, GL-$C_3N_4$, $SnO_2$/GL-$C_3N_4$ composites.

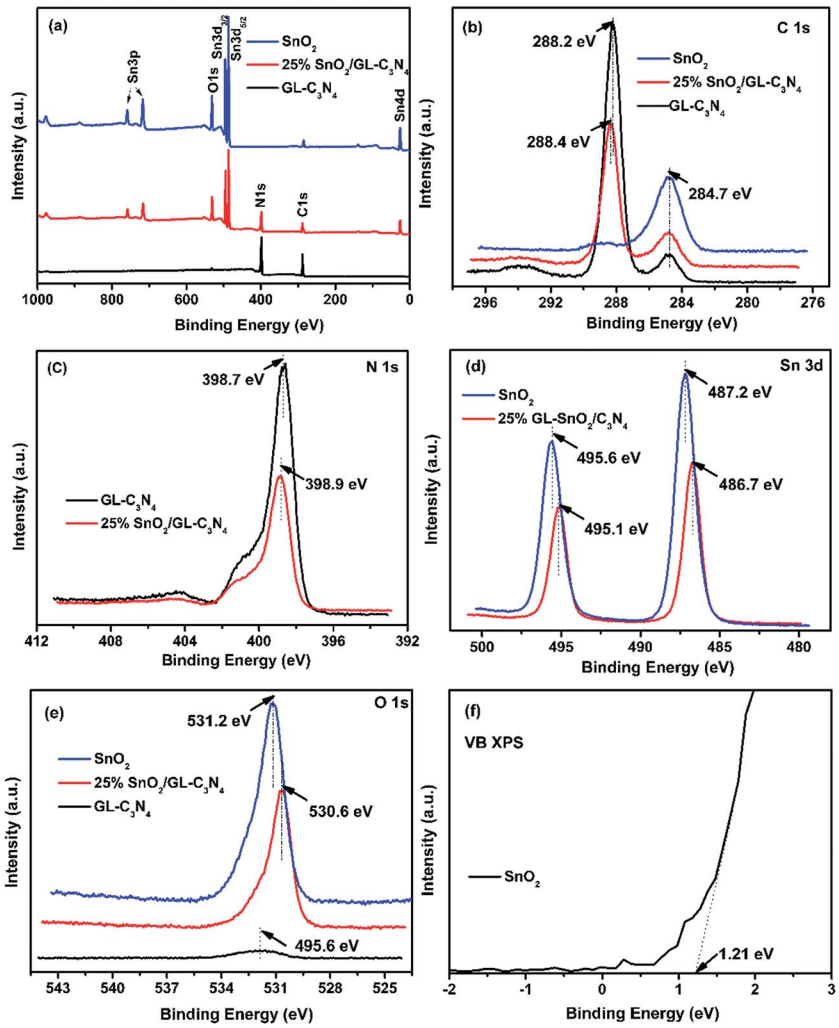


Fig. 2 XPS spectra of $SnO_2$, GL-$C_3N_4$ and 25 wt% $SnO_2$/GL-$C_3N_4$ composite, (a) survey spectra, (b) C 1s, (c) N 1s, (d) Sn 3d, (e) O 1s, (f) VB XPS of $SnO_2$.

attributed to the strong interactions between $SnO_2$ and GL-$C_3N_4$ which had influenced the chemical environments of N–C=N. Fig. 2(c) showed that the N 1s peak located at 398.7 eV in GL-$C_3N_4$ originated from C=N–C coordination[37] was shift to 398.9 eV in 25 wt% $SnO_2$/GL-$C_3N_4$ composite proving that there was existing an interaction between $SnO_2$ and GL-$C_3N_4$. The binding energy of Sn 3d peaks in $SnO_2$ located at 495.6 and 487.2 eV were ascribed to Sn $3d_{5/2}$ and Sn $3d_{3/2}$ of $Sn^{4+}$ oxidation state, respectively[39] (Fig. 2(d)). Obviously, the corresponding Sn 3d peaks of 25 wt% $SnO_2$/GL-$C_3N_4$ were shift to 495.1 and 486.7 eV, respectively. The shift providing evidence of the interactions between $SnO_2$ and GL-$C_3N_4$. The O 1s peak in $SnO_2$ at 531.2 eV should be ascribed to Sn–O–Sn (lattice O),[21] which changed to 530.6 eV in 25 wt% $SnO_2$/GL-$C_3N_4$ also demonstrating that there were some interactions between $SnO_2$ and GL-$C_3N_4$ (Fig. 2(e)). Fig. 2(f) showed the VB X-ray photoelectron spectra of $SnO_2$, which was 1.21 eV. The valence band value of as-prepared $SnO_2$ was different from that of normal $SnO_2$ in previous works. The cause of this phenomenon was discussed in detail in DRS section. Together with FT-IR and XRD results we knew that, GL-$C_3N_4$, $SnO_2$ and $SnO_2$/GL-$C_3N_4$ were successfully prepared in this work, and there were interactions between $SnO_2$ and GL-$C_3N_4$ in $SnO_2$/GL-$C_3N_4$ composites.

### 3.3. SEM and TEM analyses

Fig. 3 displayed typical SEM and TEM images of $SnO_2$, GL-$C_3N_4$, 25 wt% $SnO_2$/GL-$C_3N_4$ composite as well as the elemental mapping, EDS of 25 wt% $SnO_2$/GL-$C_3N_4$ composite, HRTEM images of pure $SnO_2$ and 25 wt% $SnO_2$/GL-$C_3N_4$. As shown in Fig. 3(a) and (f), GL-$C_3N_4$ was a fewer layered structure similar to the structure of graphene, which was consistent with previous reports.[33] Fig. 3(b), (g) and (i) showed SEM image, TEM image, HRTEM image recorded from frame marked region in (g) of bulk $SnO_2$, respectively. While it could be seen in Fig. 3(b) that, $SnO_2$ exhibited layer structure formed by the tiny pieces with size smaller than that of GL-$C_3N_4$. Fig. 3(g) and (i) showed that the synthesized $SnO_2$ lamellar nanosheets had irregular shape and size, which were unlike normal 2D $SnO_2$ (ref. 29 and 40) nanosheets (which had complete crystallization, thin and

 

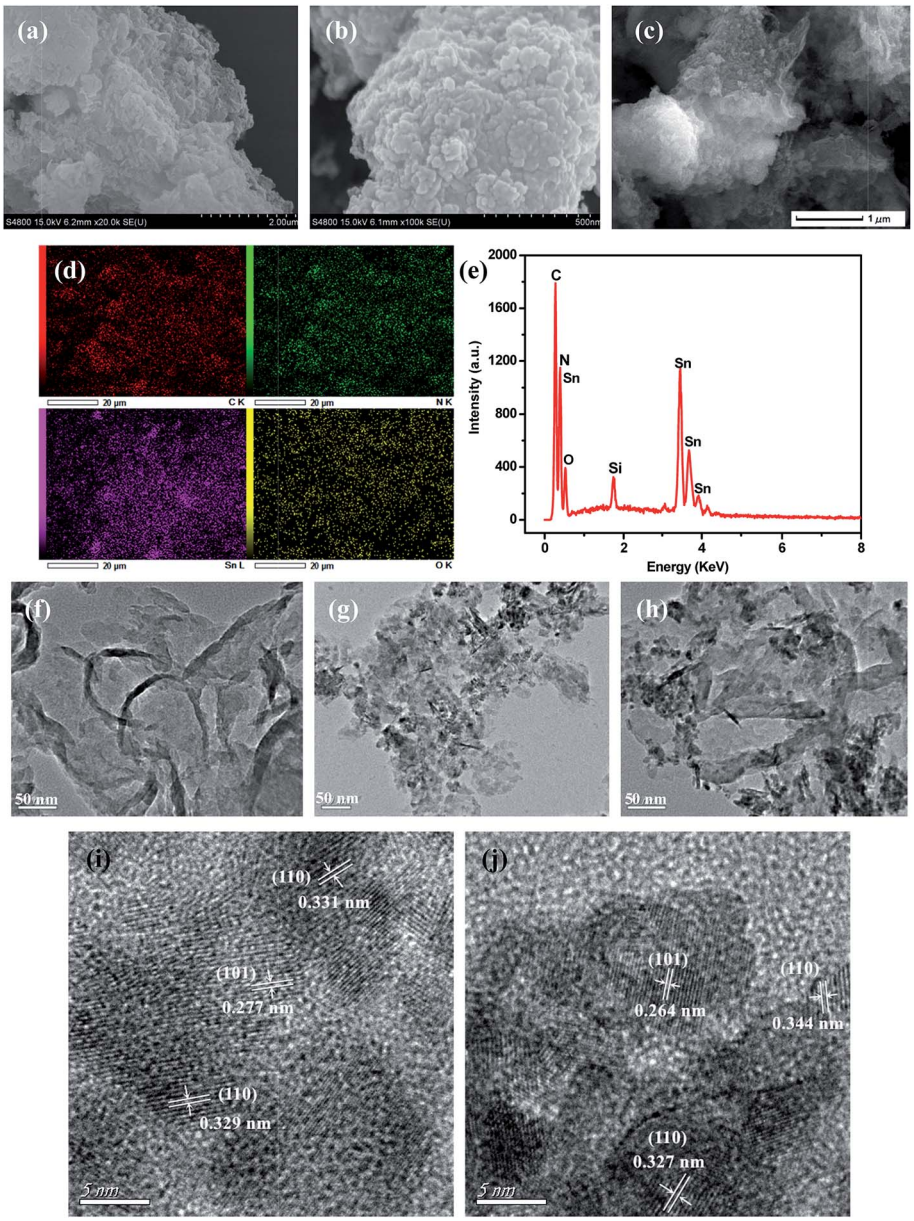


Fig. 3 SEM images: (a) GL-$C_3N_4$, (b) $SnO_2$, (c) 25 wt% $SnO_2$/GL-$C_3N_4$; (d) Elemental mapping of 25 wt% $SnO_2$/GL-$C_3N_4$, (e) EDS of 25 wt% $SnO_2$/GL-$C_3N_4$; TEM images: (f) GL-$C_3N_4$, (g) $SnO_2$, (h) 25 wt% $SnO_2$/GL-$C_3N_4$; HRTEM images of (i) pure $SnO_2$, (j) 25 wt% $SnO_2$/GL-$C_3N_4$.

structured morphology). The lattice spacing of $SnO_2$ nanosheet were estimated to be near 0.27 nm, 0.33 nm, and corresponding to the (101), (110) plane of $SnO_2$, respectively (Fig. 3(i)). So the irregular shape of the synthesized $SnO_2$ nanosheets may be caused by the incomplete crystallization which could due to the uneven cooling in Teflon-lined autoclave. Fig. 3(c), (h) and (j) were SEM image, TEM image, HRTEM image recorded from frame marked region in (h) of 25 wt% $SnO_2$/GL-$C_3N_4$ composite, respectively. As expected, the 25 wt% $SnO_2$/GL-$C_3N_4$ composite exhibited nanosheets structure and in which $SnO_2$ was wrapped around GL-$C_3N_4$, indicating that both $SnO_2$ and GL-$C_3N_4$ were exfoliated by this hydrothermal method. While the presence of $SnO_2$ may have influenced the exfoliating of g-$C_3N_4$ into 2D GL-$C_3N_4$, this caused GL-$C_3N_4$ to have loose structure and smaller size.[41] As shown in Fig. 3(j), GL-$C_3N_4$ displayed large area without crystal lattice and the interplanar spacing were estimated to be near 0.27 nm, 0.33 nm, and corresponding to the (101), (110) plane of $SnO_2$, verifying the existence of GL-$C_3N_4$ and $SnO_2$ nanosheets in 25 wt% $SnO_2$/GL-$C_3N_4$. Moreover, the interaction of $SnO_2$ and GL-$C_3N_4$ brought them a close integration, and the intimate contact between $SnO_2$ and GL-$C_3N_4$ would lead to a close interface between the two semiconductors. And this close interface allowed for the charge transfer between $SnO_2$ and GL-$C_3N_4$, promoting the separation of photoinduced electrons and holes, and increased the visible light photocatalytic activity of composites consequently. The elemental mapping and EDS (Fig. 3(d) and (e)) indicated that the 25 wt% $SnO_2$/GL-$C_3N_4$ composite containing C, N, Sn and O elements,

verifying the existence of GL-$C_3N_4$ and $SnO_2$ nanosheets in 25 wt% $SnO_2$/GL-$C_3N_4$. And the elemental mapping of elements C, N, Sn and O were uniformly distributed throughout the whole region of 25 wt% $SnO_2$/GL-$C_3N_4$ composite shown in Fig. 3(d). Those results gave reliable evidence that $SnO_2$ nanosheets were successfully combined with GL-$C_3N_4$, forming the typical 2D/2D structure which was presumed to play an important part in promoting the photo-induced electrons and holes transfer across the $SnO_2$ and GL-$C_3N_4$ contact interface, hence reducing the recombination of photoinduced electron–hole carriers.

### 3.4. $N_2$ adsorption–desorption and UV-vis analysis

$N_2$ adsorption–desorption isotherms in Fig. 4 were used for the analysis of BET specific surface areas of $SnO_2$/GL-$C_3N_4$ composites. It could be seen that the BET specific surface area of g-$C_3N_4$, GL-$C_3N_4$, $SnO_2$ and 25 wt% $SnO_2$/GL-$C_3N_4$ is 3.51 $m^2 g^{-1}$, 71.08 $m^2 g^{-1}$, 90.37 $m^2 g^{-1}$, 124.12 $m^2 g^{-1}$, respectively. The BET specific surface area of GL-$C_3N_4$ is much larger than that of g-$C_3N_4$, suggesting that the layered stacking g-$C_3N_4$ was exfoliated into 2D GL-$C_3N_4$ nanosheets.[15,42] $SnO_2$ has the large BET specific surface area, which could arise from its smaller lamellar structure. And automatically, the BET specific surface area of 25 wt% $SnO_2$/GL-$C_3N_4$ composite is much larger than that of pure GL-$C_3N_4$ and $SnO_2$, indicating the formation of 2D/2D structures which could effectively facilitate separation/transfer of photoinduced electron–hole pairs, and thus improve the catalytic performance.

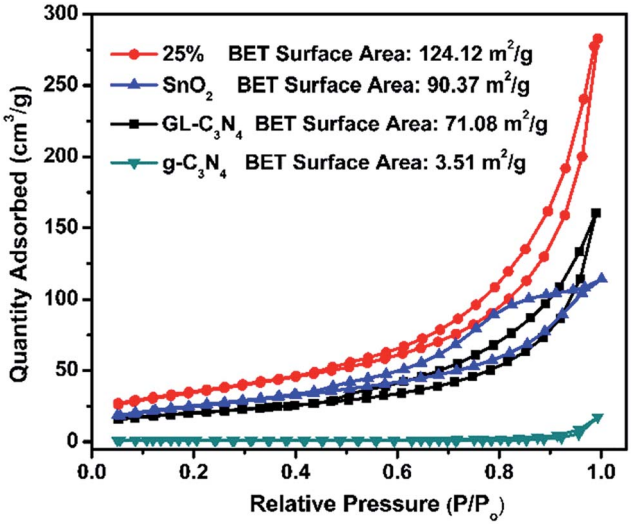


Fig. 4 $N_2$ adsorption–desorption isotherms of g-$C_3N_4$, GL-$C_3N_4$, $SnO_2$ and 25% $SnO_2$/GL-$C_3N_4$ composite.

Optical absorption property is an important parameter for the photocatalyst. UV-vis absorption spectra of $SnO_2$, GL-$C_3N_4$ and $SnO_2$/GL-$C_3N_4$ composites are shown in Fig. 5(a). It was clearly that the optical absorption edges of $SnO_2$ and GL-$C_3N_4$ were located approximately at 506 and 460 nm, respectively, which was estimated from ones absorption onset. The basal absorption edges of the $SnO_2$/GL-$C_3N_4$ composites were as similar with GL-$C_3N_4$, indicating that both Sn and O were not doped in the GL-$C_3N_4$ structure. Compared to the $SnO_2$ semicrystals,[43] $SnO_2$ nanoparticles,[44] $SnO_2$ nanotubes,[45] and other $SnO_2$ samples with the absorption edge of 305–355 nm originated from its wide band gap in previous work, the as-synthesized $SnO_2$ nanosheets in this paper showed strong visible light absorption. This result revealed that the as-prepared $SnO_2$ nanosheets had a narrow band gap and could be excited by visible light. DRS spectra are related to many factors, such as the molecular structure, color, grain size, the degree of dry of the catalyst, particularly evident influence of the color.[46] The absorption intensity in visible light region was enhanced with the increasing $SnO_2$ content in the $SnO_2$/GL-$C_3N_4$ composites which could be due to the brown color of the $SnO_2$. The optical absorption data and SEM/TEM results worked together implying that $SnO_2$ nanosheets were uniformly recombined with GL-$C_3N_4$ in this work.

The energy level and band gap of the semiconductors play crucial roles in determining these physical properties.[18] The band gap energies ($E_g$) of $SnO_2$, GL-$C_3N_4$ and $SnO_2$/GL-$C_3N_4$ composites can be estimated respectively according to the following formula eqn (2).

$$(Ahv)^2 = hv - E_g \quad (2)$$

where $A$, $h$, $v$ and $E_g$ are absorbance, Planck constant, light frequency and band gap energy, respectively. From Fig. 5(b), it could be seen that the band gap of the $SnO_2$, GL-$C_3N_4$ and 15

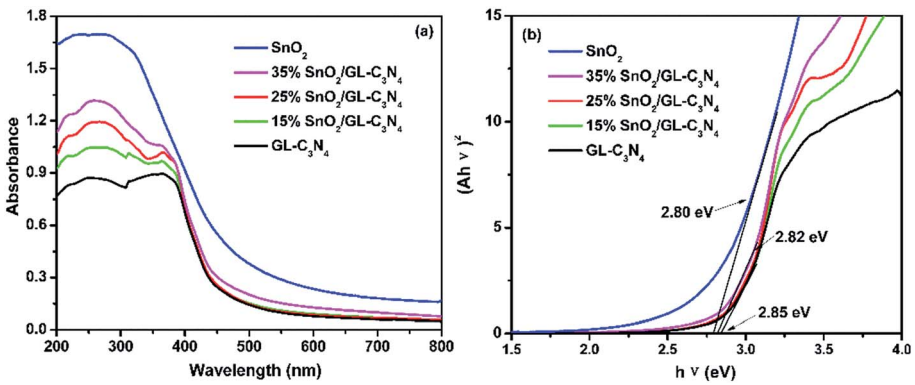


Fig. 5 (a) UV-vis diffuses reflectance spectra of the samples; (b) estimated band gap of $SnO_2$, GL-$C_3N_4$ and $SnO_2$/GL-$C_3N_4$ composites.

wt% $SnO_2$/GL-$C_3N_4$, 25 wt% $SnO_2$/GL-$C_3N_4$, 35 wt% $SnO_2$/GL-$C_3N_4$ were calculated to be ~2.80 eV, 2.85 eV, 2.85 eV and 2.82 eV, respectively. Compare to GL-$C_3N_4$, the 35 wt% $SnO_2$/GL-$C_3N_4$ composite (at high $SnO_2$ content) showed narrower band gap, which indicates that the existence of $SnO_2$ could significantly affect the energy gap. The experimental result for the $E_g$ of GL-$C_3N_4$ was in agreement with the reported literature,[13] but for $SnO_2$, the $E_g$ was significantly smaller than the literature value of 3.8 eV.[47] The reason for this phenomenon could probably be attributed to the imperfect crystallization of $SnO_2$.[48]

### 3.5. PL analysis

The PL spectra of GL-$C_3N_4$, 25 wt% $SnO_2$/GL-$C_3N_4$ in Fig. 6(a) were obtained by monitoring with an excitation wavelength of 387 nm; and $SnO_2$, 25 wt% $SnO_2$/GL-$C_3N_4$ in Fig. 6(b) were obtained by monitoring with an excitation wavelength of 275 nm. As shown in Fig. 6(a), the GL-$C_3N_4$ and 25 wt% $SnO_2$/GL-$C_3N_4$ composite presented strong PL emission at 469 nm which was corresponded to the band gap for the recombination of photogenerated electron–hole pairs.[34] Clearly, an apparent fluorescence quenching was observed for 25 wt% $SnO_2$/GL-$C_3N_4$ compared with pure GL-$C_3N_4$, indicating the suppressed recombination among photogenerated charge carriers in this photocatalyst.[49] $SnO_2$ exhibited higher emission intensity of PL spectra at 358 nm compared with 25 wt% $SnO_2$/GL-$C_3N_4$ with an commonly excitation wavelength of 275 nm.[50,51] The decreased photoluminescence intensity of 25 wt% $SnO_2$/GL-$C_3N_4$ indicating that it had lower recombination rate of photoinduced electron–hole pairs than GL-$C_3N_4$ and $SnO_2$, providing evidence of a direct effect in charge recombination between GL-$C_3N_4$ and $SnO_2$.

### 3.6. Transient photocurrents and EIS analyses

As is well known that, semiconductor with unique band gap structure may have photoelectric properties which could convert can sun light energy into electricity. And the photoelectric conversion efficiency of the $SnO_2$/GL-$C_3N_4$ could be analyzed by the photocurrent intensity of the sample. In order to further confirm the composites playing an important role in the photocatalytic reaction, four switch source loop transient photocurrent response experiment of the samples were made. In Fig. 7(a), the 25 wt% $SnO_2$/GL-$C_3N_4$ composite showed an obvious enhancement of photocurrent with respect to the bulk sample under visible light irradiation, which was almost 10 and 4 times as high as that of $SnO_2$ and GL-$C_3N_4$, respectively, indicating an improvement of charge separation. Photocurrent results confirmed that the composites had a more efficient separation of photogenerated electrons and holes. It was also confirmed that $SnO_2$ and GL-$C_3N_4$ administered together effectively at the interface and there were interactions (which playing an important role in the effective separation of electron–hole pairs of GL-$C_3N_4$) between $SnO_2$ and GL-$C_3N_4$ which was also reflected in the XPS analyses and FT-IR spectra. And 25 wt% $SnO_2$/GL-$C_3N_4$ had the highest separation efficiency of the

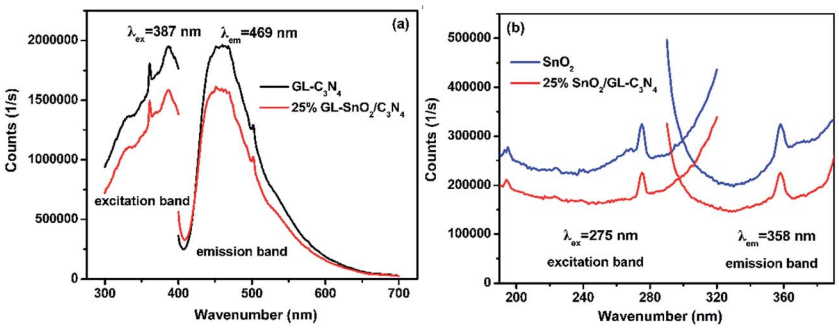


Fig. 6 PL spectra of (a) GL-$C_3N_4$, 25 wt% $SnO_2$/GL-$C_3N_4$ and (b) $SnO_2$, 25 wt% $SnO_2$/GL-$C_3N_4$.

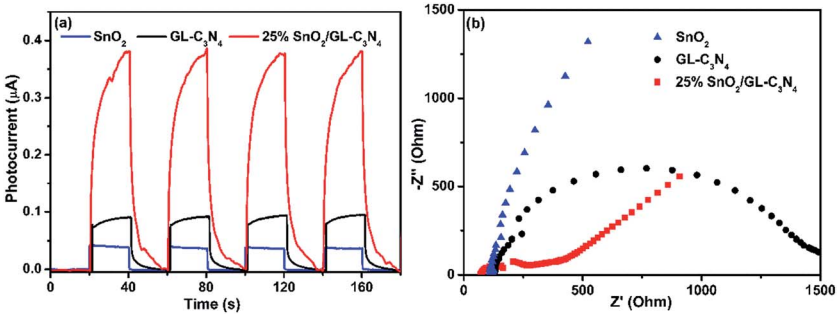


Fig. 7 (a) Transient photocurrent response for GL-$C_3N_4$, $SnO_2$ and 25 wt% $SnO_2$/GL-$C_3N_4$ composite in PBS (pH = 7.0) aqueous solution under visible light irradiation. (b) EIS of GL-$C_3N_4$, $SnO_2$ and 25 wt% $SnO_2$/GL-$C_3N_4$ composite in a 0.1 M KCl solution containing 5.0 mM $Fe(CN)_6^{3-}$/$Fe(CN)_6^{4-}$.

samples, which was in good consistent with the photocatalytic activities. The EIS measurements were conducted to gain deeper insight into the charge transport behavior of $SnO_2$/GL-$C_3N_4$ in Fig. 7(b). It has been proved that the radius of every circle in the Nyquist diagram is based on the charge transfer process at the interface of corresponding electrode/electrolyte, and the smallest radius corresponding with a lowest charge-transfer resistance.[52] It could be seen from Fig. 7(b) that there was a decline in the radius when introduced $SnO_2$ into the system, indicating that the introduction of $SnO_2$ decreased charge-transfer resistance and raised the interfacial charge transfer. Therefore, the separation of photogenerated electron–holes could be improved by combing $SnO_2$ with GL-$C_3N_4$. 25 wt% $SnO_2$/GL-$C_3N_4$ showed the smallest radius demonstrating that it had a more effective separation of photoinduced electrons and holes. EIS results were in good consistent with the four switch source loop transient photocurrent response experiment and PL spectra of the composites.

### 3.7. Photocatalytic activity test

From the characterization we mentioned above, we knew that the composites showed enhanced adsorption capability, low recombination rate and high separation efficiency. Those as-prepared composites were supposed to be efficient visible-light driven photocatalysts. The photocatalytic activities of the samples were evaluated from RhB degradation under visible light irritation. As shown in Fig. 8(a), GL-$C_3N_4$ and $SnO_2$ showed weak photocatalytic activities towards RhB degradation, of which the photocatalytic degradation efficiencies were 36% and 10%, respectively. While the degradation rate for $SnO_2$/GL-$C_3N_4$ composites (15 wt%, 25 wt%, 25 wt% physically blending, 35 wt%) under visible-light irradiation for 3 h were 88%, 92%, 78% and 71%, respectively (Fig. 8(a)). Obviously, an appropriate $SnO_2$ ratio in composite was critical significant for the improvement of the resultant photocatalytic performance. The increased photocatalytic activity of $SnO_2$/GL-$C_3N_4$ composites could be attributed to the enhanced separation efficiency of the photoexcited electron–hole pairs. For comparison, a mixture of $SnO_2$ and GL-$C_3N_4$ with an appropriate ratio of 25 wt% was also used as one of the photocatalysts. As can be seen from Fig. 8(a), the 25 wt% physically blending of $SnO_2$ and GL-$C_3N_4$ showed much lower photocatalytic activity in RhB degradation than that of 25 wt% $SnO_2$/GL-$C_3N_4$ composite. The result also indicated that there was an interaction leading to a close interface between the two semiconductors in $SnO_2$/GL-$C_3N_4$ composites. And this interaction allowed for the charge transferring between $SnO_2$ and GL-$C_3N_4$, thus promoting the separation of photoexcited electron–hole pairs, leading to a high photocatalytic activity of composites. Fig. 8(b) was the absorption spectra of 25 wt% $SnO_2$/GL-$C_3N_4$ composite in photodegradation of RhB. Under visible light irradiation for 3 h, the color of solution suspension was changed from red gradually to colorless. Also the absorption peak near 553 nm decreased gradually, which suggested that RhB was oxidation degraded completely.

### 3.8. Cycling test

The stability of the synthesized 25 wt% $SnO_2$/GL-$C_3N_4$ composite was studied by a 4-run cycling test. The photocatalytic performance of 25 wt% $SnO_2$/GL-$C_3N_4$ composite was investigated by the RhB degradation under visible light irradiation for 3 h. It could be seen from Fig. 9 that the degradation efficiency of RhB over 25 wt% $SnO_2$/GL-$C_3N_4$ after 4 recycles was very high. The stability of 25 wt% $SnO_2$/GL-$C_3N_4$ composite was

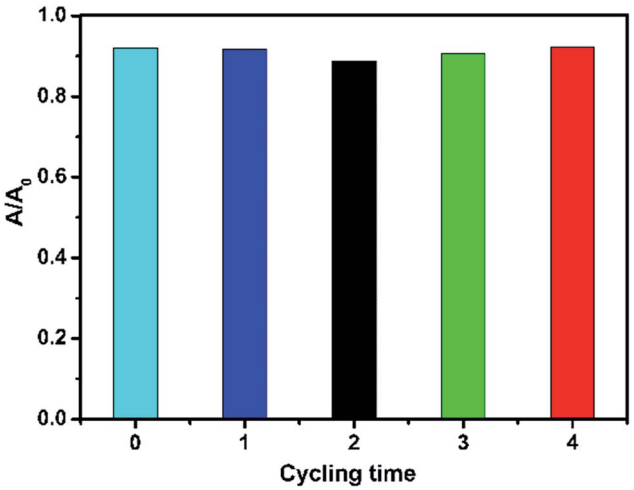


Fig. 9 The recycle test for RhB degradation over 25 wt% $SnO_2$/GL-$C_3N_4$ under visible-light irradiation.

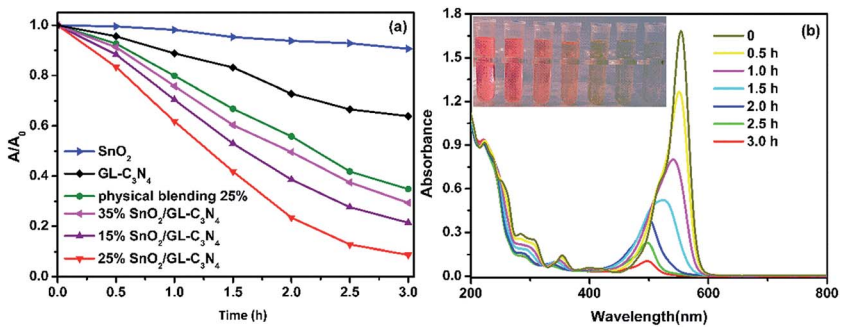


Fig. 8 (a) Photocatalytic activities of the samples for the degradation of RhB under visible-light irradiation; (b) absorption spectral changes of RhB under visible light irradiation.

 

also investigated by XRD (Fig. S1†) and FT-IR analyses (Fig. S2†). It could be seen from Fig. S1 and S2,† the recycled 25 wt% $SnO_2$/GL-$C_3N_4$ composite named "25 wt% after" had no obvious change in location compared with 25 wt% $SnO_2$/GL-$C_3N_4$ composite. These results made it clearly that 25 wt% $SnO_2$/GL-$C_3N_4$ remained effective and recyclable for RhB degradation.

### 3.9. ESR, trapping experiments and mechanism of RhB degradation under visible light

For purpose of investigate the active species produced in the photodegradation process under visible light irradiation, ESR spin-trap technique with DMPO (5,5-dimethyl-1-pyrroline-*N*-oxide) was used. As everyone knows, $H_2O_2$ was formed from photogenerated electron–hole pairs in the reactions with adsorbed water or oxygen, where $^{\bullet}OH$ and $O_2^{\bullet-}$ were possibly involved.[13] As can be shown in Fig. 10(a), $SnO_2$/GL-$C_3N_4$ treated without visible light irradiation exhibited no ESR signal. While under visible light irradiation, signals attributed to a DMPO-$O_2^{\bullet-}$ species were detected successfully in $SnO_2$/GL-$C_3N_4$ dispersions in methanolic media, indicating that $O_2^{\bullet-}$ reactive species were generated during the reaction. In addition, $^{\bullet}OH$ signals were also detected in visible light irradiation during the reaction (Fig. 10(b)). The results confirmed that both $O_2^{\bullet-}$ and $^{\bullet}OH$ were main active species.

The trapping experiments were also employed in Fig. 11, as to further study the mechanism. Usually, *t*-BuOH was employed as the part of hydroxyl radical scavenger, and 2Na-EDTA was used as holes scavenger, while $N_2$ was inlet in order to prevent $O_2^{\bullet-}$ forming.[37,53] As shown in Fig. 11, the addition of $N_2$ significantly suppressed the degradation of RhB over 25 wt% $SnO_2$/GL-$C_3N_4$ photocatalyst, while *t*-BuOH and 2Na-EDTA had suppressed the RhB degradation in varying degrees. Those results confirmed that $O_2^{\bullet-}$ was main active specie during RhB photocatalytic degradation process, which was consist with the ESR result. While $^{\bullet}OH$ and holes were also contributed part of the role in RhB photocatalytic degradation.

Fig. 12 describes the possible photocatalytic mechanism of RhB degradation over $SnO_2$/GL-$C_3N_4$ samples under visible light. The band gaps of $SnO_2$ and GL-$C_3N_4$ are 2.80 eV and 2.85 eV, respectively. Since the conduction band (CB) edge potential of $SnO_2$ is estimated as −1.59 eV and valence band (VB) is 1.21 eV. Compared with the common $SnO_2$ with wide band gap, the prepared $SnO_2$ can be excited and produces the photogenerated electron/hole pairs under visible light

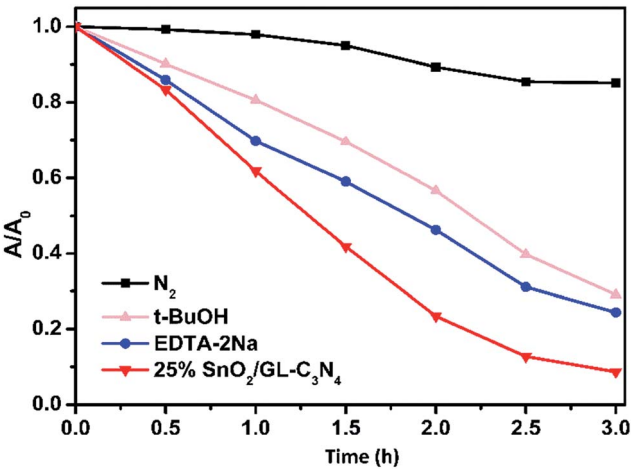


Fig. 11 Photodegradation of RhB over 25 wt% $SnO_2$/GL-$C_3N_4$ photocatalyst with different quenchers.

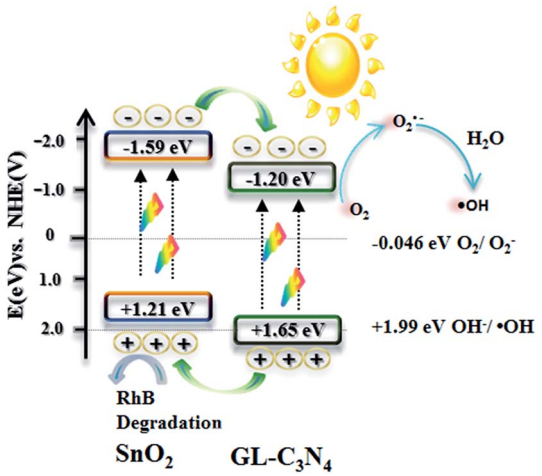


Fig. 12 Photocatalytic mechanism in the presence of $SnO_2$/GL-$C_3N_4$ under visible light.

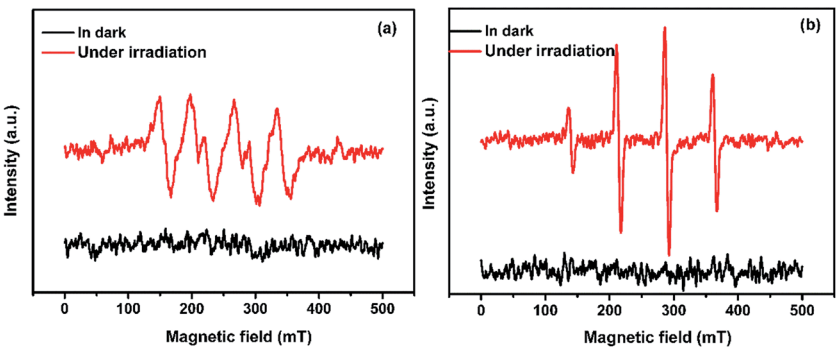


Fig. 10 ESR spectra of radical adducts trapped by DMPO: (a) DMPO-$O_2^{\bullet-}$ radical species detected for the 25 wt% $SnO_2$/GL-$C_3N_4$ dispersion in methanol, (b) DMPO-$^{\bullet}OH$ radical species detected for the 25 wt% $SnO_2$/GL-$C_3N_4$ dispersion in water.

irradiation due to its narrow band gap. While the CB and VB edge potential of GL-$C_3N_4$ are estimated to be −1.20 eV and 1.65 eV.[13] From the information mentioned above, it is clearly to know that both the CB and VB edges of GL-$C_3N_4$ are more positive than these of $SnO_2$. Therefore, when $SnO_2$/GL-$C_3N_4$ is excited under visible light irradiation, the corresponding photo-generated electrons in $SnO_2$ could easily transfer to the CB edge of GL-$C_3N_4$, while the corresponding photoinduced holes in GL-$C_3N_4$ could be easily accumulated in the VB edge of $SnO_2$. Meanwhile, the photogenerated electrons on the CB edge of GL-$C_3N_4$ can be trapped by oxygen molecules in the aqueous solution to form $O_2^{\bullet-}$ reactive oxygen species, which plays an important role in the degradation of RhB. Afterwards, part of the $O_2^{\bullet-}$ reactive oxygen species continue turning into $^{\bullet}OH$ radical and play its part in the photodegradation of RhB.[54,55] At the same time, the photogenerated holes on the VB edge of $SnO_2$ can directly oxidize RhB. Corresponds to the trapping experiments and ESR results, the photocatalytic mechanism confirmed that $O_2^{\bullet-}$, $^{\bullet}OH$ and holes worked together in combination during the RhB photodegradation process.

## 4. Conclusion

In summary, the $SnO_2$/GL-$C_3N_4$ composites were synthesized in suit by hydrothermal method using GL-$C_3N_4$ and $SnO_2$ as precursors. And 25 wt% $SnO_2$/GL-$C_3N_4$ composite showed the highest photocatalytic activity, which could degrade about 92% of RhB under visible-light irradiation within 3 h, which was almost 9 and 2.5 times higher than that of $SnO_2$ and GL-$C_3N_4$, respectively. The high photodegradation rate of RhB was ascribed to the suitable band potentials of the two components and efficient electron–hole separations *via* interface of $SnO_2$ and GL-$C_3N_4$. Moreover, the trapping experiments and ESR spectra all indicated that $O_2^{\bullet-}$, $^{\bullet}OH$ and holes worked together in combination during the photocatalytic oxidation of RhB.

## Conflicts of interest

There are no conflicts of interest to declare.

## Acknowledgements

This current work is financially supported by the National Natural Science Foundation of China (No. 21476097, 21507046), A Project Funded by the Priority Academic Program Development of Jiangsu Higher Education Institutions (PAPD).

## References

1 Y. P. Zhu, T. Z. Ren and Z. Y. Yuan, *ACS Appl. Mater. Interfaces*, 2015, **7**, 16850–16856.
2 Z. W. Zhao, Y. J. Sun and F. Dong, *Nanoscale*, 2015, **7**, 15–37.
3 F. F. Shi, L. L. Chen, C. S. Xing, D. L. Jiang, D. Li and M. Chen, *RSC Adv.*, 2014, **4**, 62223–62229.
4 X. C. Hao, X. L. Ji and Q. Zhang, *Mater. Lett.*, 2016, **185**, 29–31.
5 Y. C. Zhang, Q. Zhang, Q. W. Shi, Z. Y. Cai and Z. J. Yang, *Sep. Purif. Technol.*, 2015, **142**, 251–257.
6 Y. B. Zhao, M. Shalom and M. Antonietti, *Appl. Catal., B*, 2017, **207**, 311–315.
7 X. H. Pang, H. J. Bian, W. J. Wang, C. Liu, M. S. Khan, Q. Wang, J. N. Qi, Q. Wei and B. Du, *Biosens. Bioelectron.*, 2017, **91**, 456–464.
8 S. S. Hu, W. J. Ouyang, L. H. Guo, Z. Y. Lin, X. H. Jiang, B. Qiua and G. N. Chen, *Biosens. Bioelectron.*, 2017, **92**, 718–723.
9 J. L. Lv, K. Dai, J. F. Zhang, Q. Liu, C. H. Liang and G. P. Zhu, *Sep. Purif. Technol.*, 2017, **178**, 6–17.
10 A. K. Singh, K. Mathew, H. L. Zhuang and R. G. Hennig, *J. Phys. Chem. Lett.*, 2015, **6**, 1087–1098.
11 S. Jeong, D. Yoo, J. T. Jang, M. Kim and J. Cheon, *J. Am. Chem. Soc.*, 2012, **134**, 18233–18236.
12 Y. Y. Liu, H. Xiao and W. A. Goddard, *J. Am. Chem. Soc.*, 2016, **138**, 15853–15856.
13 J. Yan, Z. G. Chen, H. Y. Ji, Z. Liu, X. Wang, Y. G. Xu, X. J. She, L. Y. Huang, L. Xu, H. Xu and H. M. Li, *Chem.–Eur. J.*, 2016, **22**, 4764–4773.
14 X. D. Zhang, X. Xie, H. Wang, J. J. Zhang, B. C. Pan and Y. Xie, *J. Am. Chem. Soc.*, 2013, **135**, 18–21.
15 X. P. Dong and F. X. Cheng, *J. Mater. Chem. A*, 2015, **3**, 23642–23652.
16 Q. J. Xiang, J. G. Yu and M. Jaroniec, *J. Phys. Chem. C*, 2011, **115**, 7355–7363.
17 W. N. Xing, C. M. Li, Y. Wang, Z. H. Han, Y. D. Hu, D. H. Chen, Q. Q. Meng and G. Chen, *Carbon*, 2017, **115**, 486–492.
18 Z. Y. Zhang, D. L. Jiang, D. Li, M. Q. He and M. Chen, *Appl. Catal., B*, 2016, **183**, 113–123.
19 Y. Y. Liu, P. Stradins and S. H. Wei, *Sci. Adv.*, 2016, **2**, e1600069.
20 J. H. Feng, Y. Y. Li, M. D. Li, F. Y. Li, J. Han, Y. H. Dong, Z. W. Chen, P. Wang, H. Liu and Q. Wei, *Biosens. Bioelectron.*, 2017, **91**, 441–448.
21 L. X. Hu, F. Y. Chen, P. F. Hu, L. P. Zou and X. Hu, *J. Mol. Catal. A: Chem.*, 2016, **411**, 203–213.
22 H. L. Xia, H. S. Zhuang, T. Zhang and D. C. Xiao, *Mater. Lett.*, 2008, **62**, 1126–1128.
23 H. L. Xia, H. S. Zhuang, T. Zhang and D. C. Xiao, *J. Environ. Sci.*, 2007, **19**, 1141–1145.
24 S. H. Hwang, C. Kim and J. Jang, *Catal. Commun.*, 2011, **12**, 1037–1041.
25 K. Santhi, C. Rani and S. Karuppuchamy, *J. Alloys Compd.*, 2016, **662**, 102–107.
26 C. Q. Zhu, Y. Li, Q. Su, B. G. Lu, J. Q. Pan, J. W. Zhang, E. Q. Xie and W. Lan, *J. Alloys Compd.*, 2013, **575**, 333–338.
27 S. S. Bhande, E. K. Kim, D. V. Shinde, S. Patil, R. S. Mane and S. H. Han, *Int. J. Electrochem. Sci.*, 2013, **8**, 11596–11605.
28 R. Lamba, A. Umar, S. K. Mehta and S. K. Kansal, *Talanta*, 2015, **131**, 490–498.
29 C. Wang, Y. Zhou, M. Y. Ge, X. B. Xu, Z. L. Zhang and J. Z. Jiang, *J. Am. Chem. Soc.*, 2010, **132**, 46–47.
30 T. Tao, L. J. He, J. Li and Y. H. Zhang, *Mater. Lett.*, 2015, **138**, 45–47.

 

31 T. T. Li, L. H. Zhao, Y. M. He, J. Cai, M. F. Luo and J. J. Lin, *Appl. Catal., B*, 2013, **129**, 255–263.
32 S. C. Yan, Z. S. Li and Z. G. Zou, *Langmuir*, 2010, **26**, 3894–3901.
33 H. Xu, J. Yan, Y. G. Xu, Y. H. Song, H. M. Li, J. X. Xia, C. J. Huang and H. L. Wan, *Appl. Catal., B*, 2013, **129**, 182–193.
34 H. Zhao, Y. M. Dong, P. P. Jiang, H. Y. Miao, G. L. Wang and J. J. Zhang, *J. Mater. Chem. A*, 2015, **3**, 7375–7381.
35 H. D. Liu, *J. Mater. Sci.: Mater. Electron.*, 2014, **25**, 3353–3357.
36 A. Akhundi and A. Habibi-Yangjeh, *Mater. Express*, 2015, **5**, 309–318.
37 H. T. Ren, S. Y. Jia, Y. Wu, S. H. Wu, T. H. Zhang and X. Han, *Ind. Eng. Chem. Res.*, 2014, **53**, 17645–17653.
38 L. Q. Yea, J. Y. Liu, Z. Jiang, T. Y. Peng and L. Zan, *Appl. Catal., B*, 2013, **142**, 1–7.
39 Y. P. Zang, L. P. Li, X. G. Li, R. Lin and G. S. Li, *Chem. Eng. J. (Amsterdam, Neth.)*, 2014, **246**, 277–286.
40 T. J. Jiang, Z. Guo, J. H. Liu and X. J. Huang, *Electrochim. Acta*, 2016, **191**, 142–148.
41 Y. B. Li, H. M. Zhang, P. Liu, D. Wang, Y. Li and H. J. Zhao, *Small*, 2013, **9**, 3336–3344.
42 X. J. She, H. Xu, Y. G. Xu, J. Yan, J. X. Xia, L. Xu, Y. H. Song, Y. Jiang, Q. Zhang and H. M. Li, *J. Mater. Chem. A*, 2014, **2**, 2563–2570.
43 L. R. Zheng, Y. H. Zheng, C. Q. Chen, Y. Y. Zhan, X. Y. Lin, Q. Zheng, K. M. Wei and J. F. Zhu, *Inorg. Chem.*, 2009, **48**, 1819–1825.
44 T. Uddin Md, Y. Nicolas, C. Olivier, T. Toupance, L. Servant, M. M. Müller, H.-J. Kleebe, J. Ziegler and W. Jaegermann, *Inorg. Chem.*, 2012, **51**, 7764–7773.
45 C. Q. Zhu, Y. R. Li, Q. Su, B. G. Lu, J. Q. Pan, J. W. Zhang, E. Q. Xie and W. Lan, *J. Alloys Compd.*, 2013, **575**, 333–338.
46 H. Y. Ji, X. C. Jing, Y. G. Xu, J. Yan, H. P. Li, Y. P. Li, L. Y. Huang, Q. Zhang, H. Xu and H. M. Li, *RSC Adv.*, 2015, **5**, 57960–57967.
47 M. T. Niu, F. Huang, L. F. Cui, P. Huang, Y. L. Yu and Y. S. Wang, *ACS Nano*, 2010, 681–688.
48 C. Wang, J. C. Zhao, X. M. Wang, B. X. Mai, G. Y. Sheng, P. A. Peng and J. M. Fu, *Appl. Catal., B*, 2002, **39**, 269–279.
49 Y. J. Zhou, L. X. Zhang, W. M. Huang, Q. L. Kong, X. Q. Fan, M. Wang and J. L. Shi, *Carbon*, 2016, **99**, 111–117.
50 Zulfiqar, R. Khan, Y. L. Yuan, Z. Iqbal, J. Yang, W. C. Wang, Z. Z. Ye and J. G. Lu, *J. Mater. Sci.: Mater. Electron.*, 2017, **28**, 4625–4636.
51 H. Shen, X. R. Zhao, L. B. Duan, R. D. Liu, H. J. Wu, T. Hou, X. W. Jiang and H. D. Gao, *Appl. Surf. Sci.*, 2017, **391**, 627–634.
52 I. Shakir, M. Shahid and D. J. Kang, *Chem. Eng. J. (Amsterdam, Neth.)*, 2013, **225**, 650–655.
53 H. Xu, H. Z. Zhao, Y. G. Xu, Z. G. Chen, L. Y. Huang, Y. P. Li, Y. H. Song, Q. Zhang and H. M. Li, *Ceram. Int.*, 2016, **42**, 1392–1398.
54 B. Yuan, J. X. Wei, T. J. Hu, H. B. Yao, Z. H. Jiang, Z. W. Fang and Z. Y. Chu, *Chin. J. Catal.*, 2015, **36**, 1009–1016.
55 Q. Li, N. Zhang, Y. Yang, G. Z. Wang and D. H. L. Ng, *Langmuir*, 2014, **30**, 8965–8972.